Chinese Journal of
POLYMER SCIENCE

RESEARCH ARTICLE

https://doi.org/10.1007/s10118-025-3394-7
Chinese J. Polym. Sci. **2025**, *43*, 1592–1601

Compatibilizer-aided Fabrication of a 'High-entropy Polymer Blend'

Jia-Nan Du[a], Wen-Kang Wei[a], Shi-De Lu[b], and Dong Wang[a*]

[a] *State Key Laboratory of Organic-Inorganic Composites & Beijing Key Laboratory of Advanced Functional Polymer Composites, Beijing University of Chemical Technology, Beijing 100029, China*
[b] *Shandong Runde Composite Materials Co., Ltd., Tai'an 271000, China*

Electronic Supplementary Information

Abstract High-entropy polymer blends composed of polypropylene (PP), polystyrene (PS), polyamide 6 (PA6), poly(lactic acid) (PLA), and styrene-ethylene-butylene-styrene (SEBS) were successfully fabricated using maleic anhydride-grafted SEBS (SEBS-*g*-MAH) as a compatibilizer. Dynamic mechanical analysis (DMA), differential scanning calorimetry (DSC), scanning electron microscopy (SEM), and mechanical testing demonstrated that SEBS-*g*-MAH significantly enhanced the compatibility between the polar (PA6, PLA) and nonpolar (PP, PS, SEBS) components. The compatibilizer effectively refined the microstructure, substantially reduced the domain sizes, and blurred the phase boundaries, indicating enhanced interfacial interactions among all the components. The optimal compatibilizer content (15 wt%) notably increased tensile ductility (elongation at break from 5.0% to 23.7%) while maintaining balanced crystallization behavior, despite slightly decreasing modulus. This work not only demonstrates the broad applicability of high-entropy polymer blends as a sustainable strategy for converting complex, unsorted plastic waste into high-performance value-added materials that significantly contribute to plastic upcycling efforts, but also highlights intriguing physical phenomena emerging from such complex polymer systems.

Keywords Polymer blends; Compatibilization; High-entropy; Morphology

Citation: Du, J. N.; Wei, W. K.; Lu, S. D.; Wang, D. Compatibilizer-aided fabrication of a 'high-entropy polymer blend'. *Chinese J. Polym. Sci.* **2025**, *43*, 1592–1601.

INTRODUCTION

High-entropy alloys (HEAs) have emerged as a transformative concept in materials research, challenging conventional alloy design strategies by incorporating at least five principal elements in equiatomic or near-equimolar proportions.[1] This innovative approach, first introduced by Yeh *et al.* in 1995 and later refined by his 2004 work, stands in sharp contrast to traditional alloys, which typically focus on single or few components.[2–4] HEAs leverage unique effects, including the thermodynamic high-entropy effect, severe lattice distortion effect, sluggish diffusion effect, and the "cocktail effect," to achieve exceptional thermal stability. These alloys can form solid solution phases, nanostructures, or even amorphous structures, endowing them with outstanding properties, such as high strength, hardness, wear resistance, oxidation resistance, and corrosion resistance, which are rarely achieved simultaneously in conventional alloys.[5–15] Over the past few decades, significant progress has been made in the fabrication of HEAs, with most applications focusing on their mechanical properties. However, recently, their potential has expanded to include applications in magnetic,[16] invar,[17] and catalytic fields.[18] This has spurred the emergence of a new field that includes both high-entropy alloys and high-entropy ceramics and heralds exciting directions for future material innovation.[19–21]

Despite the substantial number of studies on high-entropy alloys, research on high-entropy polymer blends remains limited. This is primarily due to the fact that most disparate polymers are thermodynamically immiscible, resulting in macroscopic phase separation due to their small entropic advantage upon blending. Consequently, these blends exhibit instability and inferior properties.[22–24] To the best of our knowledge, Jr. and co-workers were the first to propose the concept of "high-entropy" polymer blend.[25] They employed solvent blending to prepare blends of a range of polymers, including polystyrene (PS), poly(methyl methacrylate) (PMMA), polycarbonate (PC), polyvinylpyrrolidone (PVP), and polyisoprene (PIP). These blends demonstrate unique and promising phenomena. For instance, they observed that the typical phase separation observed in polymer blends can be suppressed as the number of polymer species (*n*) in the blend increases. This behavior was attributed to a "high-entropy effect," in which steric hindrance from dissimilar macromolecular species prevents aggregation during film formation.[25,26] Subsequent to this work, Hirai *et al.* developed high-entropy polyamide (PA) blends using *in situ* exchange reactions, incorporating four types of aliphatic polyamides: PA6, PA610, PA11, and PA12.[27] They found that quaternary polyamide blends exhibited distinct properties, including reduced crys-

* Corresponding author, E-mail: dwang@mail.buct.edu.cn
Received April 5, 2025; Accepted June 5, 2025; Published online July 8, 2025

tallinity and increased elongation at break. The numerical analysis further revealed that the randomness of the molecular sequence in the reactive quaternary blend increased significantly during melt mixing.

Undoubtedly, the introduction of five polymer components to fabricate a high-entropy material inevitably results in complex interactions. However, there are several important reasons for the development high-entropy polymer blends. Beyond the desire to understand the interplay between the five polymer components within a single blend, there is growing concern over the environmental and economic challenges posed by plastic waste.[28,29] Recycled plastic scrap often contains a variety of polymers, which are generally difficult to sort or separate effectively. In addition, blends derived from such mixtures are typically thermodynamically immiscible, leading to poor mechanical properties.[30–32] By applying the concept of high-entropy alloys and utilizing a compatibilizer, it may be possible to transform waste plastics into high-entropy polymer blends with enhanced mechanical and physical properties. This innovative approach offers a practical and sustainable way to upcycle plastic waste, enhancing its utility and value, while addressing critical environmental concerns.[33,34]

In this study, polypropylene (PP), polystyrene (PS), polyamide 6 (PA6), polylactic acid (PLA), and poly[styrene-*b*-(ethylene-*co*-butylene)-*b*-styrene] (SEBS) were selected to fabricate high-entropy polymer blends because these polymers are typical plastic waste constituents widely encountered in daily life.[35,36] Among these components, PP, PS, PA6, and PLA are inherently immiscible, whereas PA6 and PLA have weak interfacial interactions and SEBS is compatible with PP and PS. To enhance the compatibility across these diverse polymers, maleic anhydride (MAH)-grafted SEBS (SEBS-*g*-MAH) was employed as a compatibilizer (Fig. 1). The MAH groups in SEBS-*g*-MAH can react with the hydroxyl groups of PLA and amine groups of PA6, forming block copolymers in situ and effectively bridging the polar and nonpolar phases. Furthermore, SEBS-*g*-MAH exhibits high compatibility with SEBS, PP, and PS.[37–46] Unlike traditional high-entropy polymer blends, which primarily rely on entropy-driven miscibility through multiple polymer components to suppress macroscopic phase separation,[25,26] our work uniquely integrates compatibilization strategies using SEBS-*g*-MAH as an efficient compatibilizer. As a result, the introduction of SEBS-*g*-MAH significantly improved the interfacial interactions between the polar (PA6, PLA) and nonpolar (PP, PS, SEBS) components, producing polymer blends with substantially refined microstructures and improved mechanical properties and enhanced ductility. This compatibilizer-aided strategy thus represents an advanced compatibilization approach, significantly advancing existing methodologies for high-entropy polymer systems and offering a promising route for recycling and upcycling complex mixed plastic wastes.

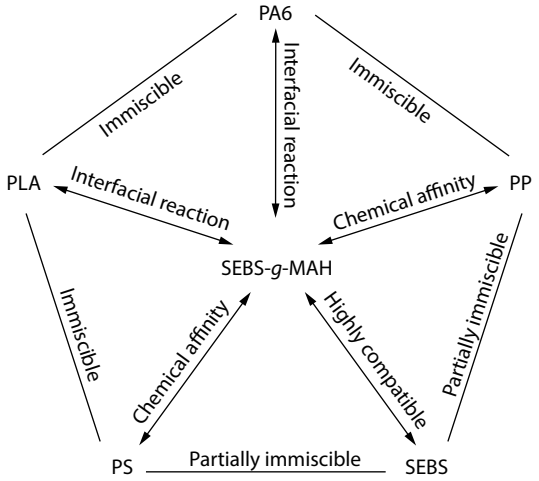

Fig. 1 Schematic illustration of the compatibilizer-aided fabrication of a high-entropy PP/PS/PA6/PLA/SEBS blend.

EXPERIMENTAL

Materials

Isotactic PP (HC600TF) with a melt, index (MFI) = 2.8 g/10min (230 °C/2.16 kg)), PLA (4032D, MFI=7.0 g/10min (230 °C/2.16 kg)), PA6 (1013B, MFI=15.8 g/10min (230 °C/2.16 kg)), PS (535, MFI=7.0 g/10min (200 °C/5.0 kg)), and SEBS (H1051, with styrene of 42 wt% and MFI=0.8 g/10min (230 °C/2.16 kg)) were obtained from Borealis, NatureWorks, UBE, Sinopec Guangzhou Petrochemical Company, and Asahi KASEI respectively. SEBS-*g*-MAH with a maleic anhydride (MAH) grafting content of 0.85 wt%, was prepared from SEBS (H1053, Asahi Kasei; 29 wt% styrene, MFI = 1.8 g/10min at 230 °C/2.16 kg) and characterized following previously reported procedures in the literature.[37,47] In a typical grafting procedure, SEBS was first premixed with an acetone solution containing MAH and DCP in a weight ratio of SEBS:MAH:DCP = 100:3:0.3. The premixed materials were subsequently introduced into a Haake torque rheometer with a 50 cm^3 chamber. Grafting reactions were conducted at 190 °C with a rotor speed of 60 r/min for 8 min.

Preparation of High-entropy PP/PS/PA6/PLA/SEBS Blends

All the blends were prepared by melt blending using a Haake torque rheometer (Rheomix QC). The mixing temperature, rotation speed, and time were 230 °C, 60 r/min, and 10 min, respectively. The mixed components were dried in a vacuum oven at 80 °C for 8 h before blending. A series of blends with compositions of PP/PS/PA6/PLA/(SEBS+SEBS-*g*-MAH) at weight ratios of 20%:20%:20%:20%:20% were prepared. The detailed compositions are listed in Table 1. The blends were pressed into thin sheets of 15 cm × 15 cm × 1 mm (length × width × thickness)

Table 1 Composition of high-entropy PP/PS/PA6/PLA/SEBS blends.

PP content (g)	PS content (g)	PA6 content (g)	PLA content (g)	SEBS content (g)	SEBS-*g*-MAH content (g)	Compatibilizer content (%)
10	10	10	10	10	0	0
10	10	10	10	7.5	2.5	5
10	10	10	10	5	5	10
10	10	10	10	2.5	7.5	15
10	10	10	10	0	10	20

using a Toyoseiki MP-SCL hot press at 230 °C and under a pressure of 10 MPa for 10 min. Subsequently, the sheets were cut into standard tensile specimens for testing.

Characterizations

Dynamic mechanical analysis (DMA)

DMA testing was performed using DMA Q850 (TA Instruments) in the single-cantilever mode. The test temperature ranged from –80 °C to 230 °C, with a heating rate of 3 °C/min. The testing frequency was 1 Hz and the strain of the samples was set to 0.1%.

Differential scanning calorimetry (DSC)

The melting and crystallization behaviors of the blends were characterized using a PerkinElmer DSC2000 instrument under a nitrogen (N_2) atmosphere. The sample (5–6 mg) was sealed in an aluminum pan and heated from room temperature to 230 °C at a rate of 10 °C/min, held for 5 min to eliminate thermal history, then cooled to 25 °C at the same rate, held for 5 min, followed by reheating to 230 °C at the same rate. The cooling and second heating curves were recorded.

Wide-angle X-ray diffraction (WAXD)

The WAXD patterns of the blends were recorded using a Rigaku Ultima IV X-ray diffractometer (XRD). The Cu K*α* radiation X-ray source was operated at a voltage of 40 kV and a current of 40 mA. The scanning range was 10° to 30° with a step size of 0.02°.

Scanning electron microscopy (SEM) observations

The blend morphologies were analyzed using a JEOL JSM-7800F SEM at an acceleration voltage of 10 kV. The blend samples were cryogenically fractured and coated with gold using a sputtering coater. To study the distribution of different phases in the blends, the cryogenically fractured surfaces were selectively etched at room temperature for 24 h using formic acid, NaOH, tetrahydrofuran (THF), and n-heptane, which correspond to the good solvents of the PA6, PLA, PS, and SEBS phases, respectively.

Tensile and flexural testing

Tensile tests were conducted on dumbbell-shaped specimens using a Shimadzu AGS-X universal testing machine at room temperature at a crosshead speed of 50 mm/min. The flexural properties were evaluated using three-point bending tests performed using the same universal testing machine at a crosshead speed of 1 mm/min at room temperature. To ensure the reliability and reproducibility of the results, at least five specimens were tested for each sample in both tensile and flexural experiments.

RESULTS AND DISCUSSION

Dynamic Mechanical Analysis

Dynamic mechanical analysis (DMA) was performed to assess the compatibilizing effect of SEBS-*g*-MAH in high-entropy PP/PS/PA6/PLA/SEBS blends. Fig. 2 and Fig. S1 (in the electronic supplementary information, ESI) show the loss factor (tan*δ*) curves as a function of temperature; the corresponding T_g values are summarized in Table 2 and Table S1 (in ESI). As shown in Fig. 2, five distinct peaks appear in the order of increasing temperature, corresponding to the T_g of SEBS, PP, PA6, PLA, and PS, respectively.[41,48] The first peak, attributed to the ethylene–butylene (EB) segments in SEBS, increases from –34.7 °C to –28.5 °C as the compatibilizer content increases from 0 wt% to 20 wt%. The second peak, associated with the T_g of PP, shows a marked decrease from 18.1 °C to 6.8 °C. The third peak is assigned to PA6, whose T_g increases from 72.0 °C to 74.0 °C when compatibilizer content increases from 0 wt% to 10 wt%. The fourth peak, corresponding to the T_g of PLA, decreases from 99.4 °C to 93.4 °C within the same compatibilizer range (0 wt%–10 wt%). A higher compatibilizer content led to the disappearance of a distinct T_g for both PA6 and PLA, which was replaced by a broad peak situated between their initial positions. The final peak, attributed to the T_g of PS, shifts slightly upward from 125.3 °C to 126.8 °C as the compatibilizer content increases from 0 wt% to 20 wt%.

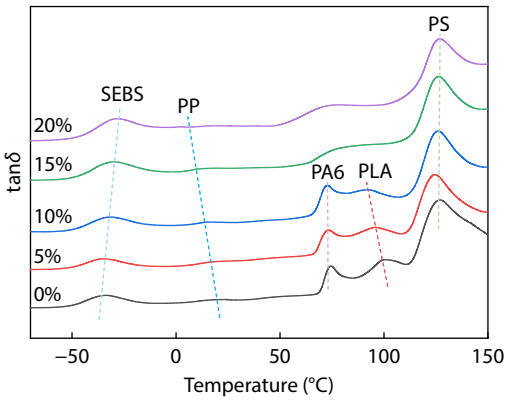

Fig. 2 tan*δ* curves as a function of temperature for the high-entropy PP/PS/PA6/PLA/SEBS blends with varying compatibilizer contents.

It is evident that the SEBS-*g*-MAH compatibilizer significantly influences the T_g of SEBS, PP, PA6, PLA, and PS in the PP/PS/PA6/PLA/SEBS blends. The increase in T_g of SEBS is primarily attributed to the reactions between the anhydride groups of SEBS-*g*-MAH and the hydroxyl groups of PLA, as well as the amine groups of PA6, resulting in the formation of SEBS-*g*-PLA and SEBS-*g*-PA6 copolymers.[49–53] These reactions improve the dispersion of SEBS and enhance its interfacial bonding with PLA and PA6, consequently restricting the mobility of the EB segments and increasing the T_g of SEBS. For

Table 2 T_g of SEBS, PP, PA6, PLA, and PS in high-entropy PP/PS/PA6/PLA/SEBS blends with varying compatibilizer contents.

Compatibilizer content (%)	T_g (°C)					MFR (230 °C, 2.16 kg)
	SEBS	PP	PA6	PLA	PS	
0	–34.7	18.1	72.0	99.4	125.3	21.1±0.8
5	–33.7	17.5	72.9	95.7	125.5	12.5±0.6
10	–31.7	14.7	74.0	93.4	125.7	9.8±0.4
15	–30.1	10.5	76.4		126.2	5.1±0.5
20	–28.5	6.8	72.8		126.8	4.3±0.2

https://doi.org/10.1007/s10118-025-3394-7

the T_g of PP, it decreases from 18.1 °C to 6.8 °C, whereas that of PS slightly increases from 125.3 °C to 126.8 °C upon the incorporation of SEBS-*g*-MAH, despite the total SEBS segment content (SEBS + SEBS-*g*-MAH) remains constant. This opposite T_g shift for PP and PS is attributed to the significantly altered microtopology and interfacial interactions within the multiphase blends. Specifically, as the anhydride groups react with the amine groups of PA6 and the hydroxyl groups of PLA, the resulting copolymers anchor the SEBS segments at the polar interfaces. Consequently, partial rubbery EB blocks protrude deeper into adjacent nonpolar PP-rich domains. This intimate intermixing increases the local free volume and enhances the segmental mobility of PP, thereby effectively reducing its T_g. Conversely, for PS, the two styrene end-blocks of SEBS-*g*-MAH preferentially interacted and anchored within the PS phase, causing partial EB segments to stretch outwards toward the nonpolar (PP) interfaces (some EB segments toward the polar PA6 and PLA interfaces due to copolymer formation). As a result, the PS domains lose a partial fraction of the flexible EB segments and instead become more rigidly interconnected by styrene segments anchored at both ends to the neighboring PA6 and PLA phases. This reduction in local free volume and increase in intermolecular interactions restrict the segmental mobility of PS, leading to a slight elevation in T_g. For PA6, the T_g slightly increases from 72.0 °C to 74.0 °C, primarily arises from the formation of rigid and strongly polar amide linkages between the amine groups of PA6 and the anhydride groups of SEBS-*g*-MAH, significantly restricting the segmental mobility of the PA6 chains. Furthermore, these newly formed covalent bonds enhance intermolecular hydrogen bonding among the PA6 chains, thereby further limiting the chain mobility and resulting in an elevated T_g. Conversely, the decrease in T_g observed for PLA (from 99.4 °C to 93.4 °C) can be attributed to the ester linkages formed between PLA hydroxyl groups and SEBS-*g*-MAH. Unlike the rigid amide bonds formed with PA6, these ester linkages were relatively more flexible. Additionally, the elastomeric nature of the SEBS segments of the SEBS-*g*-PLA copolymers acts effectively as an internal plasticizer, increasing the free volume within the PLA-rich domains, disrupting its crystalline order, and facilitating molecular mobility. Consequently, this reduces the T_g of the PLA. At elevated SEBS-*g*-MAH loadings, the distinct T_g peaks of PA6 and PLA disappeared and merged into a broad peak, indicating enhanced chain miscibility and a significant reduction in interfacial tension, reflecting a highly compatibilized state. These results demonstrate that SEBS-*g*-MAH employs diverse compatibilization mechanisms, increasing T_g for SEBS, PA6, and PS by restricting chain motion and lowering T_g for PP and PLA through enhanced plasticization. At higher compatibilizer loadings, the merging of the distinct T_g of PA6 and PLA signifies a more compatibilized blend structure. Additionally, the MFR results (Table 2) showed a consistent decrease in MFR and a corresponding increase in melt viscosity with increasing compatibilizer loading. Together with the TGA results, which reveal an increase in T_{max} (the temperature at the maximum mass loss rate) from 441 °C without compatibilizer to 451.8 °C with 15 wt% SEBS-*g*-MAH (Fig. S2 in ESI). These findings further support the formation of copolymers and intensified interfacial interactions created by SEBS-*g*-MAH.

Crystallization and Melting Behavior

The high-entropy PP/PS/PA6/PLA/SEBS blends contained three crystalline components, PP, PA6, and PLA, whose intricate crystallization interactions significantly influenced the crystal structure, crystal form, crystallinity, and melting temperature, ultimately affecting the mechanical performance of the blends. The impact of the SEBS-*g*-MAH compatibilizer on the crystallization and melting behavior of these blends is presented in the DSC curves in Fig. 3, with the relevant crystallization parameters (crystallization temperature T_c and melting temperature T_m) summarized in Table 3. Without the compatibilizer, the DSC cooling curves exhibit three distinct crystallization peaks at approximately 82.6, 107.5, and 186.5 °C, corresponding to PLA, PP, and PA6, respectively. Complex interactions among these crys-

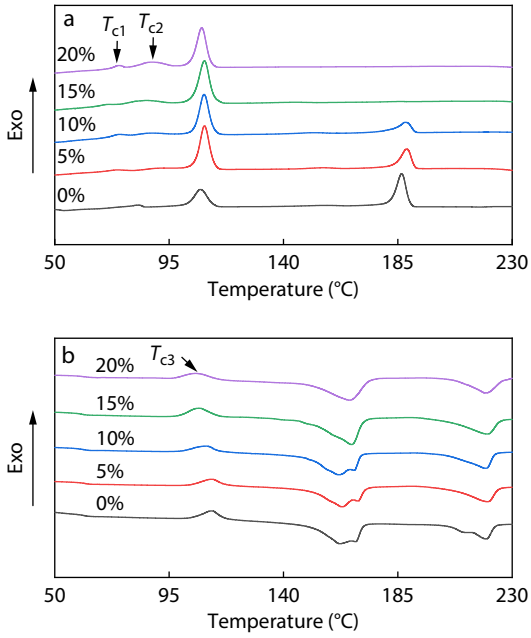

Fig. 3 Crystallization (a) and second heating (b) curves of high-entropy PP/PS/PA6/PLA/SEBS blends with varying compatibilizer contents.

Table 3 Crystallization and melting data of high-entropy PP/PS/PA6/PLA/SEBS blends with varying compatibilizer contents.

Compatibilizer content (%)	PP			PLA				PA6			
	T_c (°C)	T_m (°C)	ΔH_m (J/g)	T_{c1} (°C)	T_{c2} (°C)	T_{c3} (°C)	T_m (°C)	T_c (°C)	T_m (°C)		ΔH_m (J/g)
0	107.5	168.9	16.6	–	82.6	112.0	162.1	186.5	210.6	219.7	13.3
5	108.7	168.6	17.3	74.9	88.7	111.9	162.5	188.0	219.6		12.6
10	108.8	168.1	18.0	74.2	87.8	109.7	163.2	188.5	219.4		12.0
15	108.9	166.8	23.4	70.3	85.9	107.1	–	–	219.3		10.3
20	107.9	166.1	17.8	74.9	87.9	105.8	–	–	219.2		9.3

https://doi.org/10.1007/s10118-025-3394-7

talline phases lead to multiple crystal forms and melting behaviors.

In particular, PLA displays a melting peak (T_m) at 162.1 °C, PP at 168.9 °C, while PA6 exhibits two melting peaks at 210.6 and 219.7 °C, which correspond respectively to its *γ*-form (observed at 21.2° in WAXD) and *α*-form (observed at 20.3° and 23.6° in WAXD), as shown in Fig. 4. Additionally, during the heating scans, a prominent exothermic peak around 112 °C (T_{c3}) was observed, indicating the cold crystallization phenomenon characteristic of PLA.

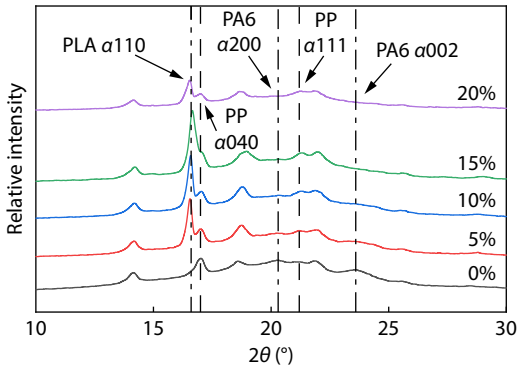

Fig. 4 XRD patterns of high-entropy PP/PS/PA6/PLA/SEBS blends with varying compatibilizer contents.

The addition of the SEBS-*g*-MAH compatibilizer significantly altered the crystallization and melting behavior, as well as the crystal form. With only 5 wt% SEBS-*g*-MAH, PLA demonstrates fractionated crystallization, evidenced by two distinct crystallization peaks at 74.9 °C (T_{c1}) and 88.7 °C (T_{c2}). This behavior arises from an in situ interfacial reaction between the PLA hydroxyl groups and MAH groups of SEBS-*g*-MAH, forming SEBS-*g*-PLA copolymers.[49–51] These copolymers significantly enhanced PLA dispersion, creating well-distributed heterogeneous nuclei and promoting interfacial-induced crystallization, as indicated by the higher T_c and the distinct appearance of the *α* (110) crystal plane at 16.5° in the WAXD profiles (Fig. 4). Conversely, the cold crystallization temperature (T_{c3}) decreases with increasing compatibilizer content due to residual amorphous PLA segments confined within thinner interfacial layers and plasticized by the rubbery EB blocks, gaining mobility at lower temperatures, thus facilitating earlier crystallization upon reheating. Similarly, chemical reactions between the amine groups of PA6 and MAH groups on SEBS-*g*-MAH form SEBS-*g*-PA6 copolymers,[52,53] dramatically reducing the size of the PA6 domains and thereby enhancing the crystallization of PA6. This phenomenon was evidenced by an increase T_c and the absence of the *γ*-form melting peak. When the compatibiliser content reached 15 wt%, the PA6 crystallization peak disappears completely, accompanied by the absence of *α* (200) and *α* (002) reflections (at 20.3° and 23.6°) (Fig. 4), indicative of strong confined crystallization. Due to the higher reactivity between amine groups and anhydride groups compared to hydroxyl groups, the PA6 component primarily reacts with SEBS-*g*-MAH, forming abundant SEBS-*g*-PA6 copolymers and resulting in the uniform dispersion of PA6 into tiny droplets (see SEM observations). Consequently, PA6 crystallization was significantly constrained, predominantly producing the *γ*-crystal form (Fig. 4). Additionally, the melting peak observed at 219.3 °C in DSC heating curves corresponds to the transformation of the metastable *γ*-form to the more stable *α*-form upon heating. Further increasing the compatibilizer content progressively enhanced PLA crystallization, achieving a maximum crystallization ability at 15 wt% SEBS-*g*-MAH (Fig. 4). For PP, the addition of the compatibilizer did not affect its crystal form, but effectively promoted crystallization, as demonstrated by the increased T_c and melting enthalpy (ΔH_m), with the greatest enhancement observed at 15 wt% compatibilizer loading. At high compatibilizer loadings (20 wt%), extensive encapsulation of PP crystals by the thickened SEBS-rich interphase and increased penetration of rubbery EB blocks dilute crystallizable PP segments, elevate melt viscosity, and restrict PP chain mobility, collectively hindering lamellar growth and thus reducing the T_c of PP.

Microscopic Phase Morphology Observations

To investigate the morphology of the high-entropy PP/PS/PA6/PLA/SEBS blends, the cryogenically fractured surfaces were selectively etched using formic acid, NaOH, THF, and *n*-heptane, which effectively dissolved PA6, PLA, PS, and SEBS. PP was not etched because its typical solvents, such as xylene, require high temperatures and would also dissolve PS and SEBS, complicating SEM observations. Fig. 5 and Fig. S3 (in ESI) show the cryo-fractured and etched morphologies of the blends with varying compatibilizer contents. In the absence of the SEBS-*g*-MAH (Fig. 5a) compatibilizer, the fracture surface exhibited multiple large, discrete domains (tens of micrometers in size) embedded within a continuous matrix, indicating poor interfacial adhesion between the polar (PA6, PLA) and nonpolar (PP, PS, SEBS) components. Although the EB segments of SEBS are compatible with PP and its styrene segments with PS, the absence of chemical coupling ultimately led to the blend remaining immiscible. Selective etching with formic acid removes the PA6 phase, leaving large, circular, or oval voids (average domain size of 22.8 μm, Table S2 in ESI) that show PA6 poorly bonded to the surrounding domains (Fig. 5b). Similarly, NaOH etching removes the PLA phase and also reveals relatively large voids (average size of 45.1 μm) (Fig. 5c and Table S2 in ESI), confirming that PLA exists as large and discrete domains with limited interfacial bonding. Thus, it was confirmed from Figs. 5(b) and 5(c) that PA6 and PLA remained relatively large and isolated domains, respectively. However, a close inspection of Fig. 5(c) also reveals that some PA6 particles were partially encapsulated by PLA, forming a core-shell-like structure. This can be attributed to hydrogen bonding between the hydroxyl groups in PLA and the amine groups in PA6, as well as dipole-dipole interactions between these two polar phases. Due to PA6's higher surface energy compared to that of PLA, PLA tends to encapsulate PA6. Etching with *n*-heptane selectively dissolved the SEBS phase, revealing irregular yet somewhat continuous pores (Fig. 5d). This morphology suggests that SEBS was dispersed throughout the PP and PS matrix, driven by the compatibility of its styrene segments with PS and EB segments with PP. The PS phase, etched by THF, appeared as irregularly dispersed pores (Fig. 5e), loosely bonded to the surrounding matrix (PP, PA6, and PLA), once again indicating relatively weak interfacial adhesion despite compatibility with SEBS styrene segments. Overall, the uncompatibilized blend system displays a typical "sea-island" morphol-

https://doi.org/10.1007/s10118-025-3394-7

ogy characterized by large immiscible phases, poor interfacial adhesion, and distinct phase separation, which is consistent with the expected results of blending several incompatible polymers without a compatibilizer.

With the addition of SEBS-*g*-MAH compatibilizer at 5 wt% (Fig. S3a in ESI) and 10 wt% (Fig. 5a′), a notable transformation in the phase morphology of PP/PS/PA6/PLA/SEBS blends is observed. The size of the dispersed domains is significantly reduced to below about 5 μm, resulting in a rougher and more irregular fracture surface compared to the smooth surface seen without the compatibilizer. This reduction in domain size and blurring of phase boundaries indicate enhanced interfacial adhesion and improved compatibility among the blend components. Selective etching with formic acid, which specifically removes PA6, exposes uniformly distributed smaller voids (approximately 2.0 μm at 10 wt% compatibilizer), indicating that PA6 droplets become finer and are better anchored within the matrix, due to chemical reactions

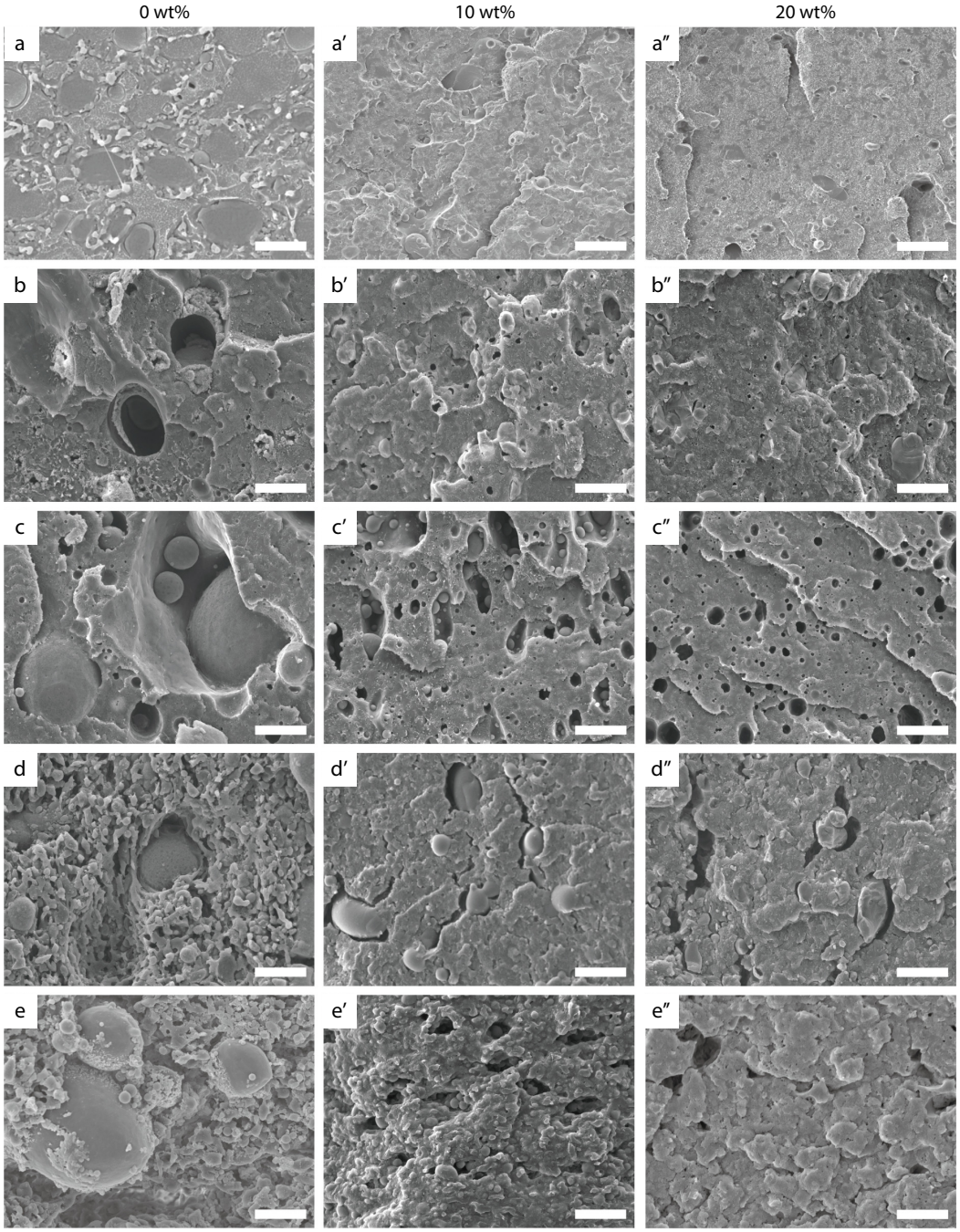

Fig. 5 SEM images of high-entropy PP/PS/PA6/PLA/SEBS blends with 0 wt% (a–e), 10 wt% (a′–e′), and 20 wt% (a″–e″) SEBS-*g*-MAH loading. (a–a″) cryofractured surface, (b–b″) cryofractured and PA6 phase extracted with formic acid, (c–c″) cryofractured and PLA phase extracted with NaOH solution, (d–d″) cryofractured and SEBS phase extracted with n-heptane, and (e–e″) cryofractured and PS phase extracted with THF. The scale bar of cryofractured surface is 5 μm, the rest are 20 μm.

https://doi.org/10.1007/s10118-025-3394-7

between MAH groups and PA6 amine groups. Similarly, etching with NaOH dissolves PLA, revealing smaller (approximately 7.1 μm at 10 wt% compatibilizer) and more evenly dispersed cavities throughout the matrix, confirming the breakup of PLA domains and stronger interfacial adhesion facilitated by reactions between MAH groups and hydroxyl groups of PLA. Notably, the encapsulation structure observed in the uncompatibilized blend (Fig. 5c) evolved significantly with the addition of the compatibilizer. Numerous smaller PA6 particles were encapsulated by the PLA phases (Fig. 5c′). Etching with n-heptane dissolves SEBS, revealing that the SEBS phase appears more finely dispersed and intimately integrated with the PP and PS phases, which is attributed to both physical compatibility (through EB segments with PP and styrene segments with PS) and chemical linkages with polar PA6 and PLA *via* MAH functionality. Etching with THF, which selectively removes PS, resulted in smaller voids, further confirming the refined dispersion and enhanced integration of PS into the polymer matrix. Improved interfacial bonding, promoted by the styrene segments in SEBS-*g*-MAH and potential interactions between MAH groups and PA6/PLA, led to a finer PS distribution. Overall, these observations (Figs. 5a′–5e′ and Figs. S3a–S3e in ESI) confirm that the incorporating of 5 wt%–10 wt% SEBS-*g*-MAH substantially refines domain sizes, enhances compatibility, and establishes a more uniform, stable, and compatibilized microstructure in high-entropy PP/PS/PA6/PLA/SEBS blends.

At high compatibilizer loadings (15 wt% and 20 wt%), the fracture surface exhibits increasingly fine and homogeneous dispersion, indicating significantly enhanced dispersion and stronger interfacial adhesion among the components. The phase boundaries observed at lower compatibilizer contents became indistinguishable, signifying superior compatibility and interfacial integration. Formic acid etching shows that the PA6 domains are extremely small (approximately 0.8 μm at 20 wt% compatibilizer) and uniformly distributed, with voids becoming barely visible. This suggests that PA6 was further broken down into fine particles that were well embedded in the matrix owing to strong interfacial interactions *via* MAH and amine reactions. Similarly, NaOH etching demonstrates significantly refined and finely dispersed PLA domains (approximately 2.0 μm at 20 wt% compatibilizer), with no evident encapsulation of PA6 by PLA, indicating that PLA has similarly undergone substantial interfacial interaction and droplet breakup. Following n-heptane etching, the resulting morphology exhibited fine dispersion of SEBS within the polymer matrix. This indicates an effective interaction between SEBS and nonpolar components (PP and PS), alongside partial chemical reactions *via* MAH with polar phases (PA6 and PLA), resulting in a highly interfacial bonded phase structure. Furthermore, after THF etching, the fracture surface showed a uniform and strongly adhered morphology, suggesting substantial integration of PS within the matrix, driven by enhanced compatibility through the styrene segments in SEBS-*g*-MAH. Therefore, as SEBS-*g*-MAH increased to 15 wt% or 20 wt%, the blends exhibit dramatically reduced domain sizes and significantly enhanced interfacial compatibility among PP, PS, PA6, PLA, and SEBS components, confirming the highly effective compatibilization.

Mechanical Properties

The influence of the SEBS-*g*-MAH compatibilizer on the mechanical properties of the high-entropy PP/PS/PA6/PLA/SEBS blends was evaluated using tensile testing. Fig. 6(a) shows the stress-strain curves, and the corresponding results are summarized in Table 4 and illustrated in Fig. 6(b). Notably, all the blends lost their yielding behavior. This phenomenon primarily resulted from the refined multiphase morphology and compatibilization effects introduced by the SEBS and SEBS-*g*-MAH compatibilizers. Specifically, these compatibilizers significantly enhance interfacial adhesion and compatibility, resulting in finer disper-

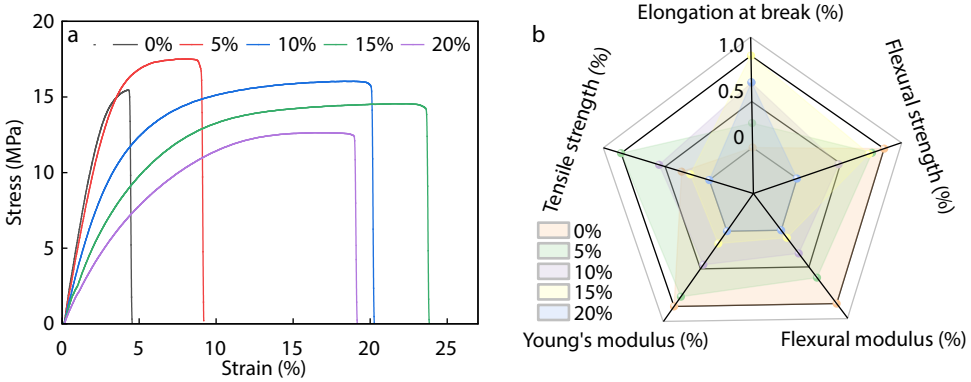

Fig. 6 (a) Stress-strain curves of high-entropy PP/PS/PA6/PLA/SEBS blends with varying compatibilizer contents; (b) Normalized mechanical properties for the blends.

Table 4 Mechanical properties of the high-entropy PP/PS/PA6/PLA/SEBS blends.

Compatibilizer content (%)	Young's modulus (MPa)	Tensile strength (MPa)	Elongation at break (%)	Flexural strength (MPa)
0	637±18	16.1±1.0	5.0±0.9	22.5±0.7
5	571±23	17.7±0.2	8.7±0.1	21.3±0.2
10	436±9	15.7±0.5	19.6±0.6	18.0±0.4
15	354±53	14.3±0.4	23.7±0.2	21.0±0.3
20	270±11	12.6±0.1	19.0±0.2	13.9±0.1

https://doi.org/10.1007/s10118-025-3394-7

sion of various polymer phases and more homogeneous deformation. Consequently, the stress distribution and energy dissipation become more efficient throughout the blends, effectively reducing local stress concentrations and thus diminishing or eliminating the distinct yielding behavior typically observed.

With increasing compatibilizer content, the Young's modulus consistently decreased, from 637.0 MPa at 0 wt% compatibilizer to 270.0 MPa at 20 wt%. This decrease occurred because of the increased rubber content introduced by the SEBS-*g*-MAH component. Specifically, SEBS-*g*-MAH (made from SEBS H1053 with 29 wt% styrene) has a higher EB rubber fraction compared to SEBS H1051 component (42 wt% styrene). Therefore, even though the total SEBS content (SEBS + SEBS-*g*-MAH) remains constant, an increase in the proportion of SEBS-*g*-MAH, which is richer in the flexible rubber segment, results in decreased stiffness and a corresponding reduction in Young's modulus. At 5 wt% compatibilizer loading, tensile strength increases from 16.1 MPa (0 wt%) to 17.7 MPa, attributed to reduced dispersed domain sizes and improved interfacial adhesion, facilitating efficient stress transfer within the blend. Beyond 5 wt%, tensile strength gradually declines, reaching 12.6 MPa at 20 wt%, which can be explained by excessive incorporation of the rubbery compatibilizer creating overly flexible interfaces, thereby weakening the load-bearing capability of the blend. In addition, constrained crystallization may further contribute to this decline. The elongation at break greatly improved with increasing SEBS-*g*-MAH content, rising dramatically from 5.0% at 0 wt% to a maximum of 23.7% at 15 wt%, indicating effective toughening due to improved interfacial interactions and enhanced stress dissipation capacity. However, at 20 wt% compatibilizer loading, elongation slightly decreases to 19.0%, suggesting an optimal concentration at around 15 wt%, beyond which the excessive compatibilizer may lead to confined crystallization or excessively flexible domains, thus reducing overall ductility. The flexural strength shows a continuous decline from 22.5 MPa at 0 wt% to 13.9 MPa at 20 wt%, paralleling the trend observed for Young's modulus. These results demonstrate that the addition of the SEBS-*g*-MAH compatibilizer significantly improves the ductility of the high-entropy polymer blends, optimally at approximately 15 wt%, while balancing other mechanical properties such as tensile strength, and modulus.

Considering the interaction mechanism between the different component pairs and the observed SEM morphologies, a schematic illustration of the phase morphology with 15 wt% SEBS-*g*-MAH compatibilizer is presented in Fig. 7. Within this morphology, the nonpolar components (PP and PS) formed irregular, ribbon-like sub-networks percolating throughout the blend. The rubbery EB segments from SEBS and SEBS-*g*-MAH interact with these ribbons, effectively plasticizing the PP domains, which results in a decreased T_g for PP, whereas the styrene end-blocks anchor strongly within the PS domains, causing a slight increase in the T_g of PS. The polar PA6 and PLA phases were finely dispersed into micron and submicron droplets and substantially confined by chemically bonded SEBS-*g*-PA6 and SEBS-*g*-PLA copolymers at their interfaces, promoting heterogeneous nucleation and confined crystallization. Specifically, PA6 predominantly formed isolated droplets, some of which were partially encapsulated by PLA domains. The compatibilizer-rich interphase, comprising both SEBS-*g*-MAH and residual SEBS, continuously coated the polar/nonpolar interfaces, significantly reducing the interfacial tension and increasing T_c of PLA and initially of PP, but eventually restricting PP lamellar growth at high loading. This elastic interphase not only merges the distinct glass transitions of PA6 and PLA into a single broad transition but also improves the tensile ductility and toughness by uniformly dissipating stress throughout the well-connected and compatibilized network.

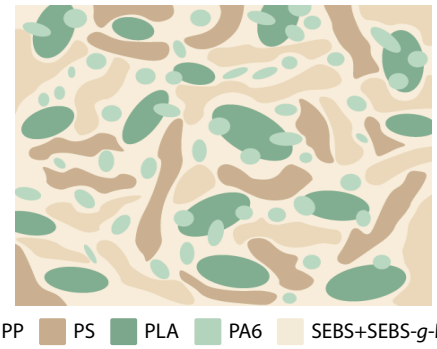

Fig. 7 Schematic illustration of the phase morphology with 15 wt% SEBS-*g*-MAH compatibilizer.

CONCLUSIONS

The compatibilizing effect of SEBS-*g*-MAH in high-entropy PP/PS/PA6/PLA/SEBS blends was systematically evaluated. DMA analysis confirmed compatibilizer-induced variations in glass transition behavior, signifying substantial improvements in interfacial interactions and compatibility. DSC investigations revealed enhanced nucleation and crystallization behavior, particularly for PLA and PA6, attributable to the formation of chemically bonded copolymers and confined crystallization effects at higher compatibilizer loadings. Morphological analysis further verified the reduction in phase domains, improved distribution uniformity, and strengthened interfacial adhesion with increasing SEBS-*g*-MAH content. Mechanical testing revealed a significant improvement in ductility, particularly at the optimal compatibilizer loading of 15 wt%, balancing mechanical strength and flexibility effectively. Overall, the incorporation of SEBS-*g*-MAH represents an effective strategy for fabricating and tailoring high-entropy polymer blends, highlighting their potential applications in plastic recycling and upcycling. This approach can effectively transform complex, unsorted plastic waste mixtures containing various polymers into value-added, high-performance polymer blends, thereby offering promising solutions for sustainable plastic waste management.

Conflict of Interests

The authors declare no interest conflict.

Electronic Supplementary Information

Electronic supplementary information (ESI) is available free of charge in the online version of this article at http://doi.org/

10.1007/s10118-025-3394-7.

Data Availability Statement

The data supporting the findings of this study are available from the corresponding author upon request.

ACKNOWLEDGMENTS

This work was financially supported by the National Natural Science Foundation of China (No. 52173017) and the Project of Introducing Urgently Needed and Scarce Talents in Key Supported Regions of Shandong Province in 2024.

REFERENCES

1 George, E. P.; Raabe, D.; Ritchie, R. O. High-entropy alloys. *Nat. Rev. Mater.* **2019**, *4*, 515–534.
2 Yeh, J. W.; Chen, S. K.; Lin, S. J.; Gan, J. Y.; Chin, T. S.; Shun, T. T.; Tsau, C. H.; Chang, S. Y. Nanostructured high-entropy alloys with multiple principal elements: novel alloy design concepts and outcomes. *Adv. Eng. Mater.* **2024**, *6*, 299–303.
3 Yeh, J. W.; Lin, S. J.; Chin, T. S.; Gan, J. Y.; Chen, S. K.; Shun, T. T.; Tsau, C. H.; Chou, S. Y. Formation of simple crystal structures in Cu-Co-Ni-Cr-Al-Fe-Ti-V alloys with multiprincipal metallic elements. *Metall. Mater. Trans. A* **2024**, *35*, 2533–2536.
4 Cantor, B.; Chang, I. T. H.; Knight, P.; Vincent, A. J. B. Microstructural development in equiatomic multicomponent alloys. *Mater. Sci. Eng. A* **2004**, *375-377*, 213-218.
5 Geng, Y. S.; Chen, W. Y.; Tan, H.; Cheng, J.; Zhu, S. Y.; Yang, J.; Liu, W. M. Remarkable wear resistance in a complex concentrated alloy with nanohierarchical architecture and composition undulation. *Research* **2023**, *6*, 0160.
6 Wei, Q.; Xu, X.; Shen, Q.; Luo, G.; Zhang, J.; Li, J.; Fang, Q.; Liu, C. T.; Chen, M.; Nieh, T. G.; Chen, J. Metal-carbide eutectics with multiprincipal elements make superrefractory alloys. *Sci. Adv.* **2022**, *8*, eabo2068.
7 Yang, T.; Zhao, Y. L.; Li, W. P.; Yu, C. Y.; Luan, J. H.; Lin, D. Y.; Fan, L.; Jiao, Z. B.; Liu, W. H.; Liu, X. J.; Kai, J. J.; Huang, J. C.; Liu, C. T. Ultrahigh-strength and ductile superlattice alloys with nanoscale disordered interfaces. *Science* **2022**, *369*, 427–432.
8 Xin, B.; Zhang, A.; Han, J.; Meng, J. The tribological properties of carbon doped $Al_{0.2}Co_{1.5}CrFeNi_{1.5}Ti_{0.5}$ high entropy alloys. *Wear* **2021**, *484–485*, 204045.
9 Li, T.; Wang, S.; Fan, W.; Lu, Y.; Wang, T.; Li, T.; Liaw, P. K. CALPHAD-aided design for superior thermal stability and mechanical behavior in a TiZrHfNb refractory high-entropy alloy. *Acta Mater.* **2023**, *246*, 118728.
10 Liu, Y.; Ren, J.; Guan, S.; Li, C.; Zhang, Y.; Muskeri, S.; Liu, Z.; Yu, D.; Chen, Y.; An, K.; Cao, Y.; Liu, W.; Zhu, Y.; Chen, W.; Mukherjee, S.; Zhu, T.; Chen, W. Microstructure and mechanical behavior of additively manufactured CoCrFeMnNi high-entropy alloys: Laser directed energy deposition versus powder bed fusion. *Acta Mater.* **2023**, *250*, 118884.
11 Kadirvel, K.; Fraser, H. L.; Wang, Y. Microstructural design *via* spinodal-mediated phase transformation pathways in high-entropy alloys (HEAs) using phase-field modelling. *Acta Mater.* **2023**, *243*, 118438.
12 Ma, S.; Liu, W.; Li, Q.; Zhang, J.; Huang, S.; Xiong, Y.; Xu, B.; Yang, T.; Zhao, S. Mechanism of elemental segregation around extended defects in high-entropy alloys and its effect on mechanical properties. *Acta Mater.* **2024**, *264*, 119537.
13 Xiong, F.; Liu, X.; Wang, H.; Jiang, S.; Rempel, A. A.; Zhang, X.; Wu, Y.; Lu, Z. Strengthening $Al_{0.1}$CoCrFeNi high-entropy alloy *via* multiaxial cryogenic forging and low temperature annealing. *Materialia* **2024**, *34*, 102086.
14 Zhang, C.; Yu, Q.; Tang, Y. T.; Xu, M.; Wang, H.; Zhu, C.; Ell, J.; Zhao, S.; MacDonald, B. E.; Cao, P.; Schoenung, J. M.; Vecchio, K. S.; Reed, R. C.; Ritchie, R. O.; Lavernia, E. J. Strong and ductile FeNiCoAl-based high-entropy alloys for cryogenic to elevated temperature multifunctional applications. *Acta Mater.* **2023**, *242*, 118449.
15 Hilhorst, A.; Jacques, P. J.; Pardoen, T. Towards the best strength, ductility, and toughness combination: high entropy alloys are excellent, stainless steels are exceptional. *Acta Mater.* **2023**, *260*, 119280.
16 Luo, W.; Li, Y.; Zou, Q.; Dai, L.; Ren, H.; Jia, H.; Luo, Y. A. The role of Cu element in $Fe_{9.4}Co_{6.7}Ni_{6.6}Mn_{0.9}V_{0.9}Cu_{2.4}$ magnetic high-entropy alloys. *Mater. Sci. Eng. A* **2024**, *912*, 147005.
17 Liu, L.; Huang, S.; Vitos, L.; Dong, M.; Bykova, E.; Zhang, D.; Almqvist, B. S. G.; Ivanov, S.; Rubensson, J. E.; Varga, B.; Varga, L.K.; Lazor, P. Pressure-induced magnetovolume effect in CoCrFeAl high-entropy alloy. *Commun. Phys.* **2019**, *2*, 42.
18 Ma, M.; Li, L.; Tian, G.; Geng, Z.; Zhang, X.; Zhao, X.; Li, G. Creation of surface frustrated Lewis pairs on high-entropy spinel nanocrystals that boosts catalytic transfer hydrogenation reaction. *Chem. Eng. J.* **2023**, *470*, 144291.
19 Yeh, J. W.; Lin, S. J. Breakthrough applications of high-entropy materials. *J. Mater. Res.* **2018**, *33*, 3129–3137.
20 Liaw, P. K.; Li, W. High entropy materials: challenges and prospects. *Metals* **2021**, *11*, 1643.
21 Wang, Y.; Zhang, J.; Wu, T.; Huang, G. Full-scale insight into high-entropy ceramics from basic concepts, synthesis technologies, structural characteristics, and properties to application prospects. *J. Mater. Res. Technol.* **2024**, *33*, 398–430.
22 Eisele, U. *Introduction to Polymer Physics, Springer-Verlag*. Berlin, **1990**, p.99–p.106.
23 Sperling, L. H. *Introduction to Physical Polymer Science*. Wiley, Somerset, **2015**, p.145–p.195.
24 Hou, X.; Chen, S.; Koh, J. J.; Kong, J.; Zhang, Y. W.; Yeo, J. C. C; Chen, H.; He, C. Entropy-driven ultratough blends from brittle polymers. *ACS Macro Lett.* **2021**, *10*, 406–411.
25 Huang, Y. J.; Yeh, J. W.; Yang, A. C. M. "High-entropy polymers": a new route of polymer mixing with suppressed phase separation. *Materialia* **2021**, *15*, 100978.
26 Huang, Y. J.; Yeh, J. W.; Yang, A. C. M. Photonics of high-entropy polymers revealing molecular dispersion *via* polymer mixing. *ACS Nano* **2024**, *18*, 32759–32768.
27 Hirai, T.; Yagi, K.; Nakai, K.; Okamoto, K.; Murai, D.; Okamoto, H. High-entropy polymer blends utilizing *in situ* exchange reaction. *Polymer* **2022**, *240*, 124483.
28 Wang, H.; Zhang, Y.; Wang, C. Surface modification and selective flotation of waste plastics for effective recycling—a review. *Sep. Purif. Technol.* **2019**, *226*, 75–94.
29 Roland Geyer, J. R. J.; Law, K. L. Production, use, and fate of all plastics ever made. *Sci. Adv.* **2018**, *7*, e1700782.
30 Paul, D. R. Polymer Blends. Academic Press, New York, **1978**.
31 Paul, D. R.; Bucknall, C. Polymer blends: formulation & performance, Wiley, New York, **2000**.
32 Koning, C.; Van Duin, M.; Pagnoulle, C.; Jerome, R. Strategies for compatibilization of polymer blends. *Prog. Polym. Sci.* **1998**, *23*, 707–757.
33 Castro, J.; Westworth, X.; Shrestha, R.; Yokoyama, K.; Guan, Z. B.;

Efficient and robust dynamic crosslinking for compatibilizing immiscible mixed plastics through *in situ* generated singlet nitrenes. *Adv. Mater.* **2024**, *36*, e2406203.
34 Garcia J. M.; Robertson, M. L. The future of plastics recycling. *Science* **2018**, *358*, 870–872.
35 Al-Salem, S. M.; Antelava, A.; Constantinou, A.; Manos, G.; Dutta, A. A review on thermal and catalytic pyrolysis of plastic solid waste (PSW). *J. Environ. Manage.* **2017**, *197*, 177–198.
36 Cossu, R.; Lai, T. Automotive shredder residue (ASR) management: an overview. *Waste Manage.* **2015**, *45*, 143–151.
37 Wang, D.; Li, Y.; Xie, X. M.; Guo, B. H. Compatibilization and morphology development of immiscible ternary polymer blends. *Polymer* **2011**, *52*, 191–200.
38 Wang, D.; Xie, X. M. Novel strategy for ternary polymer blend compatibilization. *Polymer* **2006**, *47*, 7859–7863.
39 Wilkinson, A. N.; Clemens, M. L.; Harding, V. M. The effects of SEBS-g-maleic anhydride reaction on the morphology and properties of polypropylene/PA6/SEBS ternary blends. *Polymer* **2004**, *45*, 5239–5249.
40 Omonov, T. S.; Harrats, C.; Groeninckx, G. Co-continuous and encapsulated three phase morphologies in uncompatibilized and reactively compatibilized polyamide 6/polypropylene/polystyrene ternary blends using two reactive precursors. *Polymer* **2005**, *46*, 12322–12336.
41 Li, H. M.; Sui, X.; Xie, X. M. High-strength and super-tough PA6/PS/PP/SEBS quaternary blends compatibilized by using a highly effective multi-phase compatibilizer: Toward efficient recycling of waste plastics. *Polymer* **2017**, *123*, 240–246.
42 Li, H. M.; Xie, X. M. Morphology development and superior mechanical properties of PP/PA6/SEBS ternary blends compatibilized by using a highly efficient multi-phase compatibilizer. *Polymer* **2017**, *108*, 1–10.
43 Li, Y.; Wang, D.; Zhang, J. M.; Xie, X. M. Compatibilization and toughening of immiscible ternary blends of polyamide 6, polypropylene (or a propylene—ethylene copolymer), and polystyrene. *J. Appl. Polym. Sci.* **2011**, *119*, 1652–1658.
44 Li, Y.; Wang, D.; Zhang, J. M.; Xie, X. M. Influences of component ratio of minor phases and charge sequence on the morphology and mechanical properties of PP/PS/PA6 ternary blends. *Polym. Bull.* **2010**, *66*, 841–852.
45 Debolt, M. A.; Robertson, R. E. Impact strength and elongation-to-break of compatibilized ternary blends of polypropylene, nylon 66, and polystyrene. *Polym. Eng. Sci.* **2004**, *44*, 1800–1809.
46 Debolt, M. A.; Robertson, R. E. Morphology of compatibilized ternary blends of polypropylene, nylon 66, and polystyrene. *Polym. Eng. Sci.* **2006**, *46*, 385–398.
47 Li, H. X.; Russell, T. P.; Wang, D. Nanomechanical and chemical mapping of the structure and interfacial properties in immiscible ternary polymer systems. *Chinese J. Polym. Sci.* **2021**, *39*, 651–658.
48 Liu, W.; Zhang, S.; Yang, K.; Yu, W.; Shi, J.; Zheng, Q. Preparation of graphene-modified PLA/PBAT composite monofilaments and its degradation behavior. *J. Mater. Res. Technol.* **2022**, *20*, 3784–3795.
49 Cheng, S.; Li, T.; Jiang, M.; Duan, J.; Feng, L.; Gu, X.; Zhang, C. Construction of core-shell structure in PA6/ABS/SEBS blends for achieving stiffness-toughness balance. *Adv. Eng. Mater.* **2024**, 2402110.
50 Wu, Y.; Zhang, H.; Shentu, B.; Weng, Z. In situ formation of the core–shell particles and their function in toughening PA6/SEBS-*g*-MA/PP blends. *Ind. Eng. Chem. Res.* **2017**, *56*, 11657–11663.
51 Yan, D.; Li, G.; Huang, M.; Wang, C. Tough polyamide 6/core–shell blends prepared *via in situ* anionic polymerization of ε-caprolactam by reactive extrusion. *Polym. Eng. Sci.* **2013**, *53*, 2705–2710.
52 Chow, W. S.; Tham, W. L.; Poh, B. T.; Mohd Ishak, Z. A. Mechanical and thermal oxidation behavior of poly(lactic acid)/halloysite nanotube nanocomposites containing *N*,*N*′-ethylenebis-(stearamide) and SEBS-g-MA. *J. Polym. Environ.* **2018**, *26*, 2973–2982.
53 Leu, Y. Y.; Mohd Ishak, Z. A.; Chow, W. S. Mechanical, thermal, and morphological properties of injection molded poly(lactic acid)/SEBS-*g*-MAH/organo-montmorillonite nanocomposites. *J. Appl. Polym. Sci.* **2011**, *124*, 1200–1207.

https://doi.org/10.1007/s10118-025-3394-7